Degradation mechanism of Ti-6Al-2Sn-4Zr-2Mo-Si alloy exposed to solid NaCl deposit at high temperature

Clément Ciszak[a,b,*], Iman Abdallah[b,1], Ioana Popa[a], Jean-Michel Brossard[c], Aurélie Vande Put[b], Daniel Monceau[b], Sébastien Chevalier[a]

[a] ICB, UMR 6303 CNRS-Univ. Bourgogne Franche-Comté, 21078 Dijon Cedex, France
[b] CIRIMAT-ENSIACET, UMR CNRS 5085, 31030 Toulouse, France
[c] Veolia Recherche et Innovation, Zone portuaire de Limay, 291 Avenue Dreyfous-Ducas, 78520 Limay, France

Keywords:
Titanium
Alloy
SEM
TEM
High temperature corrosion
Internal oxidation

A B S T R A C T

This study focuses on the corrosion behaviour of Ti-6Al-2Sn-4Zr-2Mo-Si alloy in presence of NaCl deposit in air at 560 °C. The active oxidation mechanism at the origin of the corrosion phenomenon enhancement in presence of solid NaCl is thought to be connected to the formation of both external and internal thick oxidation areas. Thermodynamic calculations allowed showing the role played by the different alloying elements in the formation of the external oxide and detailed TEM characterisations brought new insights regarding the nature and origin of the internal oxidation area.

1. Introduction

Active oxidation is a severe degradation process. It is known to occur in different fields such as waste-to-energy conversion, materials recycling and aeronautics. Many works have been dedicated to the study of active oxidation of steels [1] and Ni-based alloys [2], in relation to their use in waste-to-energy facilities. These studies especially identified the role of the different metallic elements (Fe, Ni, Cr, Mo, Mn …) on the overall active oxidation process. Much less studies have been performed on Ti alloys, which can also be subjected to active oxidation when used in high temperature aeronautical applications. Similarly to steels and Ni-based alloys, Ti has been alloyed with several elements (such as Al, Nb, Zr …) to improve the behaviour of its alloys at high temperature [3–5], including their oxidation resistance.

High temperature oxidation of Ti and Ti-based alloys in classic conditions (e.g. in air or oxygen without any deposit) has been widely studied. Titanium has a high affinity for oxygen and oxidizes by forming an external scale composed mainly of rutile TiO_2, which grows by anionic diffusion. In case of Ti-based alloys containing Al, such as Ti-6Al-4 V or Ti-6Al-2Sn-4Zr-2Mo-Si, the outer part of the oxide layer often contains Al_2O_3 [6–12]. Furthermore, Ti and Ti-based alloys can dissolve large quantities of oxygen, up to 33 at. % for pure α-Ti. Oxygen can diffuse deep inside the metallic substrate, forming an α-Ti(O) solid solution which leads to the hardening and embrittlement of the affected region [8,13,14]. A few number of studies have evaluated the thickness of the oxygen affected zone (OAZ) in case of Ti-6Al-2Sn-4Zr-2Mo alloy. For instance, OAZ thicknesses of around 9 µm, 15 µm and 30 µm were reported for oxidations of 100 h at 650 °C [11] and 500 h at 538 °C [15] and 593 °C [15,16], respectively. These results, coupled with those obtained by Berthaud et al. [17], tend to indicate that OAZ thickness essentially depends on both time and temperature, which is confirmed by analyses of experimental data in a recent review [18].

Very few studies reported a degradation of the oxidation resistance of Ti-6Al-2Sn-4Zr-2Mo-Si alloy or close-composition alloys under solid NaCl deposits [19–23]. None of them proposed a clear mechanism. They only showed parabolic-like [21,22] or parabolic-then-linear [19] oxidation kinetics, whose weight gains appeared, in the first case, 6–10 times larger than those observed in dry air. In each case, damaged corrosion scales (porous, cracked and non-adherent) were observed. Corrosion scales also appeared layered, composed of a rather dense inner part and a rather porous outer part [19–21]. The external part of the corrosion scales was reported to be generally composed of rutile TiO_2, surmounted by a mixed Na-,Ti-rich oxide ($Na_4Ti_5O_{12}$ [10,22–26], $Na_2Ti_6O_{13}$ [23], Na_2TiO_4 [27], Na_2TiO_3 [5,20,28,29], $NaTiO_2$ [30]), whereas its internal part also included oxides of certain alloying elements (Al_2O_3, ZrO_2 and SnO_2) [19,22]. Formation of these corrosion products were often hypothesized to result from active corrosion mechanisms involving volatile chlorides [5,10,20,22–26,28–31] and, more rarely, chloride ions [19,22]. These metallic chlorides are supposed to form at the alloy|oxide interface, then to diffuse outward, reacting with

* Corresponding author at: CIRIMAT-ENSIACET, UMR CNRS 5085, 31030 Toulouse, France.
[1] Present address: Department of Engineering physics, University of Wisconsin-Madison, Madison,WI 553706, USA.

https://doi.org/10.1016/j.corsci.2020.108611

O_2 to form oxides of the different elements present in the alloy and release gaseous Cl_2. This later gas release might justify the presence of blisters and pores. Furthermore, the presence of salts on the material surface was found to strongly influence the formation of the OAZ, which is replaced in this case by an internal oxidation area [10,20,22–25,28].

Such internal oxidation area, unusual for Ti and Ti-based alloys, seems to first develop along grain boundaries of the metallic matrix, before expanding inside the grains [19,20,23,25,28–30]. In some cases, this expansion inside the metallic grains appears inhomogeneous and directional, looking like spaced oxide fingers growing in parallel directions [19,22,23]. Fan et al. [19,22] reported this internal oxidation area to be composed of TiO_2 and Ti_2O.

In our previous study dedicated to Ti-6Al-4 V alloy [10], a mechanism for the active oxidation of Ti alone was proposed. This mechanism involved the formation of a reaction intermediate in the form of gaseous $TiCl_4$, achieving transport of Ti from the metallic matrix to the oxide scale and its subsequent oxidation as soon as a critical oxygen partial pressure is reached. However, contrary to what has been done for steels [1] and Ni-alloys [2], the behaviour of alloying elements were not considered.

The aim of the present study is therefore to better understand the influence of NaCl deposit on the high-temperature oxidation behaviour of the Ti-6Al-2Sn-4Zr-2Mo-Si alloy, with a particular focus on the role played by the alloying elements and the formation of the internal oxidation area. Samples were analysed by means of X-ray diffraction (XRD) and scanning electron microscopy (SEM) coupled to energy dispersive X-ray spectroscopy (EDS). Oxygen dissolution areas were investigated through hardness and EDS measurements. A specific transmission electron microscopy (TEM) characterisation campaign involving TEM-EDS, electron energy loss spectroscopy (EELS), selected area electron diffraction (SAED) and high magnification imaging, was finally dedicated to the study of the internal oxidation area.

2. Material and methods

Ti-6Al-2Sn-4Zr-2Mo-Si alloy used in this study is a Ti-based alloy, containing 6 wt. % Al, 2 wt. % Sn, 4 wt. % Zr, 2 wt. % Mo and 0.1 wt. % Si (Table 1). It has an equiaxed microstructure composed of α (HCP) phase and β (BCC) phase. Square samples measure approximately 7 mm x 7 mm and are 4 mm thick. All the specimens were mechanically ground using SiC papers up to P600 grit [21,30–32] and were then cleaned in ethanol.

NaCl deposits were performed by spraying a saturated NaCl solution at the surface of the samples. The detailed spraying procedure was exposed previously in reference [10]. This method allows to obtain fully covering deposits of approximately 3–4 $mg.cm^{-2}$ of NaCl [10]. Samples exposed to laboratory air without and with NaCl deposit, named A and NA respectively, were oxidised in Carbolite CWF 1300 muffle furnaces at 560 °C during 600 h. Both samples were analysed through two successive steps. Surfaces were first characterized, followed by analyses of polished cross-sections. Cross-section preparation was previously described in reference [10].

Surface and cross-section analyses were performed by scanning electron microscopy (SEM) using JEOL JSM-7600 F set-up in back-scattered electron (BSE) and secondary electron (SE) contrasts. The elementary composition of corrosion products was analysed with energy dispersive X-ray spectroscopy (EDS). The crystalline structure of the corrosion products was determined by X-ray diffraction (XRD) using an Inel CPS 120 diffractometer and the Cu Kα (λ = 0.154 nm) radiation with fixed incidence angles ranging from 1° to 12° (depending on corrosion scale thickness). Vickers micro-hardness measurements were performed using a BUEHLER 1600-6100 apparatus. 10 g loads were applied, leading to indents with a diagonal lying between 5 and 10 μm. Indentations were performed over the whole thickness of the metallic material, every 10 μm near the surface (for the first 100 μm), then every 100 μm up to 500 μm and then every 500 μm until reaching the middle of the sample.

For further understanding of the internal corrosion area, a fine characterisation was performed. A cross-sectional 10 × 10 μm^2 transmission electron microscopy (TEM) lamellae of the internal oxidation area region was prepared using focused-ion beam (FIB) FEI HELIOS 600i apparatus. A systematic analysis was sequenced as follows: firstly, a general description of the observed region was done with EDS semi-quantitative analysis of selected areas, secondly electron energy loss spectroscopy (EELS) line scan probe was acquired near EDS areas for quantitative analysis of light elements such as oxygen in particular. Finally, selected area electron diffraction (SAED) patterns were recorded to identify the crystalline structure of the different compounds. Elemental and chemical characterisations (EDS and EELS respectively) were performed using JEOL cold-FEG JEM ARM 200 F apparatus operated at 200 kV equipped with Cs corrector probe of 0.078 nm spatial resolution. EELS spectra were recorded using GIF Quantum ER imaging filter with collection and convergence semi angles equal to 19.4 and 14.8 mrad, respectively. The collected spectra were acquired each 4 nm with an energy resolution of 0.5 eV determined by the full width half maximum (FWHM) of the recorded zero-loss peak. An energy dispersion of 0.1 eV/channel was chosen to acquire Ti-$L_{2,3}$ and O-K energy loss near edges spectra (ELNES). Low magnification, electron diffraction (ED) and high magnification TEM images were acquired using field emission gun FEG-TEM JEOL JEM 2100 F operated at 200 kV.

Factsage 6.4™ was used to perform thermodynamic calculations, in order to identify the role of different alloying elements on the active oxidation mechanism proposed in a previous study [10].

Table 1
Average chemical composition of the as received Ti-6Al-2Sn-4Zr-2Mo-Si alloy, obtained by EDS analysis.

Elements		Ti	Al	Sn	Zr	Mo	Si
Chemical composition	wt. %	Bal.	5.8	2.4	4.8	2.5	0.1
	at. %	Bal.	10.3	1.0	2.5	1.3	0.2

3. Results

3.1. Weight gains per unit area

The sample oxidised for 600 h at 560 °C in laboratory air (sample A) presents a small mass gain per unit area, of 0.28 ± 0.10 $mg.cm^{-2}$. This result is consistent with results obtained by McReynolds and Tamirisakandala in similar conditions of exposure [15].

The NaCl-coated sample (NA) exposed to laboratory air for 600 h at 560 °C shows a mass gain per unit area 12 times higher (3.41 ± 0.12 $mg.cm^{-2}$) than that of the sample without any deposit exposed to laboratory air under the same conditions.

3.2. Oxidation test in laboratory air without NaCl deposit (sample A)

Surface observations of the sample exposed to laboratory air at 560 °C for 600 h show a homogeneous aspect (Fig. 1a). In Fig. 1a, light regions (enriched in Mo and locally in Zr) and dark regions (enriched in Al), can be associated with the underlying β- and α-phases of the Ti-6Al-2Sn-4Zr-2Mo-Si alloy respectively. The observation of the initial alloy microstructure suggests the presence of a very thin oxide layer at the surface of the sample.

The global EDS surface analysis is presented in Table 2. It indicates the presence of Ti and O predominantly and of low quantities of Al, Zr, Sn and Mo. These results, coupled with XRD analysis (Fig. 2), indicate that in the present conditions, the material oxidation leads to the formation of TiO_2 rutile and anatase mainly (ICDD n° 00-021-1276 and ICDD n° 03-065-5714 respectively). The presence of strong signals

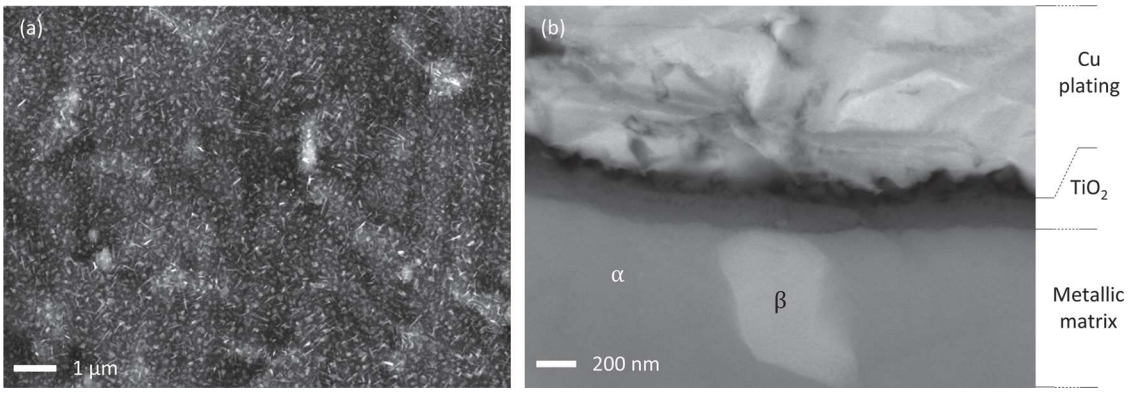

Fig. 1. Surface micrograph in SE contrast (a) and cross-section micrograph in BSE contrast (b) of sample A oxidised 600 h at 560 °C in laboratory air.

Table 2
Surface EDS analyses performed on sample A.

Sample	Content (at. %)						
	Ti	O	Al	Zr	Sn	Mo	Si
A	33.4	60.5	4.2	1.0	0.4	0.4	0.1

corresponding to α-Ti (ICDD n 00-044-1294) is another evidence of the very low thickness of the oxide layer.

Cross-section observation (Fig. 1b) confirms the previous results by revealing the presence of a very thin (~ 200 nm), dense and adherent oxide layer.

Fig. 3 presents the micro-hardness profile versus the distance from the alloy|oxide interface. Oxygen EDS profile is also depicted. Indeed, it is well known that in Ti-based alloys oxygen dissolution leads to surface hardening. Comparing micro-hardness with oxygen profile near the alloy surface is therefore a common method to determine OAZ thickness [33], although micro-hardness is more sensitive to low O contents (below 1 at. %) than EDS and EPMA [18].

A high hardness value of 530 $HV_{0.01}$ was measured in the external part of the substrate close to the alloy|oxide interface. Then the hardness value quickly decreases with the distance from the alloy|oxide interface. At around 25 µm, it reaches the average value measured for the Ti-6Al-2Sn-4Zr-2Mo-Si bulk alloy (325 $HV_{0.01}$). In parallel, the O content also decreases from 32 at. % at the interface, to 2 at. % at 10 µm from the interface. It should be noted here that because of O surface pollution (native oxide), the O contents measured by EDS are over-estimated by a few at. %. Therefore, the values mentioned above should not be considered quantitatively accurate.

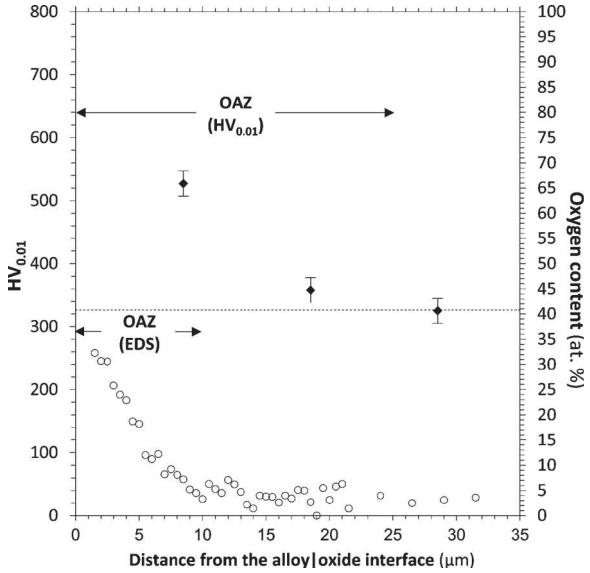

Fig. 3. Micro-hardness (◆) and relative oxygen content (○) (obtained by EDS) profiles versus distance from the alloy|oxide interface of sample A after 600 h at 560 °C in laboratory air.

3.3. Oxidation under NaCl deposit in laboratory air (sample NA)

3.3.1. Surface and cross-section analyses

Surface observations of the sample with a NaCl deposit exposed to laboratory air (NA) for 600 h at 560 °C (Fig. 4) reveal a heterogeneous

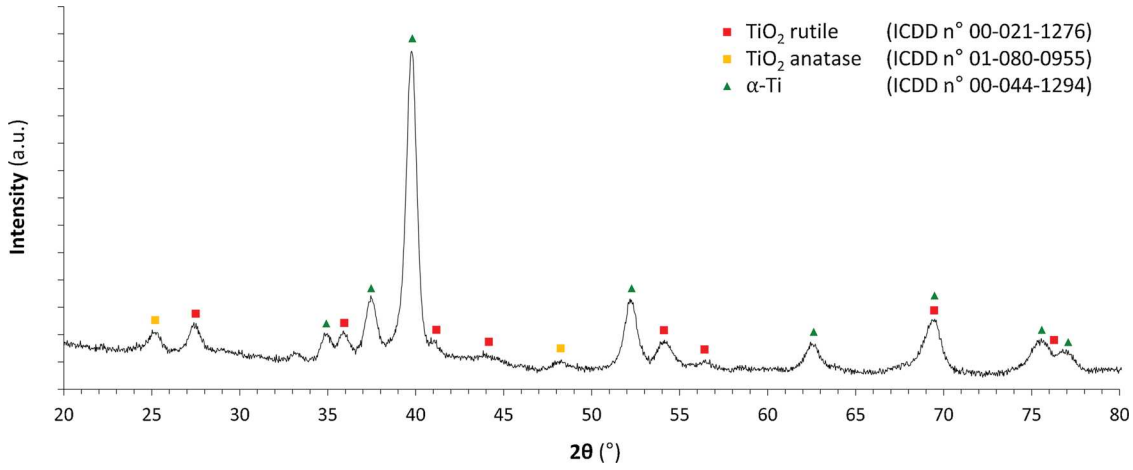

Fig. 2. Diffraction pattern of the XRD analysis performed on sample A after 600 h at 560 °C in laboratory air.

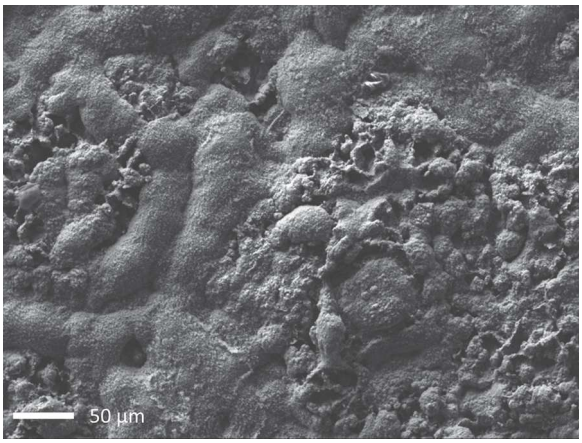

Fig. 4. Surface micrograph in SE contrast of sample NA oxidised 600 h at 560 °C in laboratory air with NaCl deposit.

Table 3
Results of surface EDS analyses performed on sample NA.

Sample	Content (at. %)		
	Ti	O	Na
NA	21.2	69.9	8.9

aspect with blisters and cracked corrosion products.

Results of EDS surface analyses are presented in Table 3. They indicate the presence of Ti and O predominantly and a small amount of Na.

Fig. 5 presents XRD analysis performed on the corrosion scale of the sample NA. For this purpose, the scale present on one side of the sample was completely removed and crushed into powder. Combining EDS non-quantitative surface chemical composition with XRD results (Fig. 5), allow to stipulate that corrosion products are mainly composed of rutile TiO_2 (ICDD n° 01-070-7347), with small amounts of $Na_4Ti_5O_{12}$ sodium-titanium mixed oxide (ICDD n° 00-052-1814). XRD pattern also indicates the presence of a zirconia-type phase (ZrO_2 (ICDD n° 01-070-2491)), doped by metallic elements of the alloy, like Al and Ti. A small amount of γ-Al_2O_3 (ICDD n° 00-047-1292) was also found.

Cross-section examination (Fig. 6a) indicates the presence of a thick (about 50 µm), cracked, porous and non-adherent oxide scale on the material surface.

EDS elementary X-ray maps (Fig. 6b–j) show that the oxide scale is composed of four different layers. The outermost part is a thin mixed sodium-titanium oxide which, according to XRD and EDS surface analyses, should correspond to hexagonal $Na_4Ti_5O_{12}$. Just below this layer, there is a very thick layer of rutile TiO_2 according to XRD results. Then, elementary X-ray maps and XRD indicate the presence of monoclinic ZrO_2-type oxide, followed by a layer of cubic γ-Al_2O_3.

Micrograph in BSE contrast (Fig. 6a) also reveals the presence of two internal corrosion areas confirmed by EDS elementary X-ray maps (Fig. 6b–j). The thickness of these internal corrosion areas reaches up to 45 µm from the alloy|oxide interface. The upper half part corresponds to a highly cracked and fully oxidised area. A small amount of Cl can be noticed at this specific location. This first zone is then followed by a partially oxidised area, depleted in Ti (as shown in Fig. 6c), which ends with large cracks and grain ravelling deep inside the metallic matrix.

Fig. 7 presents the micro-hardness profile and the relative O content versus the distance from the alloy|oxide interface. The oxygen profile appears to be constant – at an average of around 75 at. % –, along the first 25 µm, confirming the internal oxidation. Oxygen content then quickly decreases and stabilizes to around 5 at. % at approximately 50 µm from the alloy|oxide interface. Again, due to O surface pollution, the O contents measured by EDS are certainly over-estimated by a few at. %.

Unlike the previous cases of sample A, values of micro-hardness strongly decrease here when approaching the alloy|oxide interface. Micro-hardness progressively decreases from the average value of 325 $HV_{0.01}$ (for the bulk material) at 35 µm, down to 120 $HV_{0.01}$ at the alloy|oxide interface. These very low values of micro-hardness are obviously related to the cracking and grain ravelling present in this area.

Fig. 8 presents detailed micrographs in BSE and SE contrasts of the internal oxidation area in sample NA.

In agreement with O contents shown in Fig. 7, this internal oxidation area appears to be composed of a fully oxidised outer area, followed by a partially oxidised inner area. In the fully oxidised area, the equiaxed microstructure of the initial metallic matrix seems to be preserved after oxidation into TiO_2, according to Fig. 6a. This fully oxidised area also appears highly damaged: it presents many cracks and grain ravelling. Furthermore, oxidation of α grains appears to be directional, leading to a lathlike structure, as already observed by Fan et al. [19] in Ti60 alloys after exposure to NaCl solid deposit in moist air for 20 h at 600 °C. Fig. 8b and Fig. 8c, present respectively the BSE and SE images of a same grain. The absence of strong topological variations in the SE micrograph (Fig. 8c) shows that BSE contrast of the lath-like structure (observed in Fig. 8b) does not correspond to voids created by the previously mentioned loss of Ti, but rather to intra-granular chemical heterogeneity.

In the partially oxidised area, this lath-like structure appears to be more or less present in the α-grains, depending on the oxidation

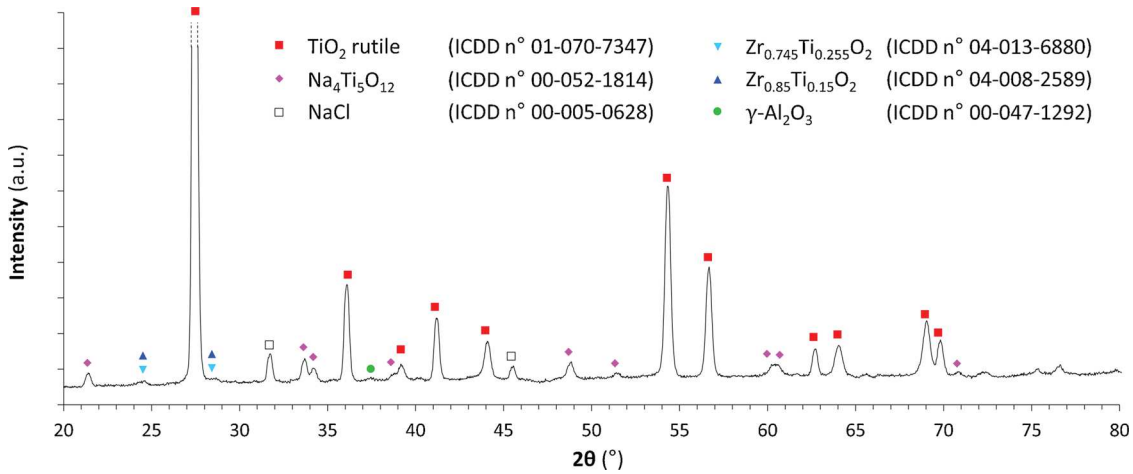

Fig. 5. Diffraction pattern of the XRD analysis performed on sample NA oxidised 600 h at 560 °C in laboratory air with NaCl deposit.

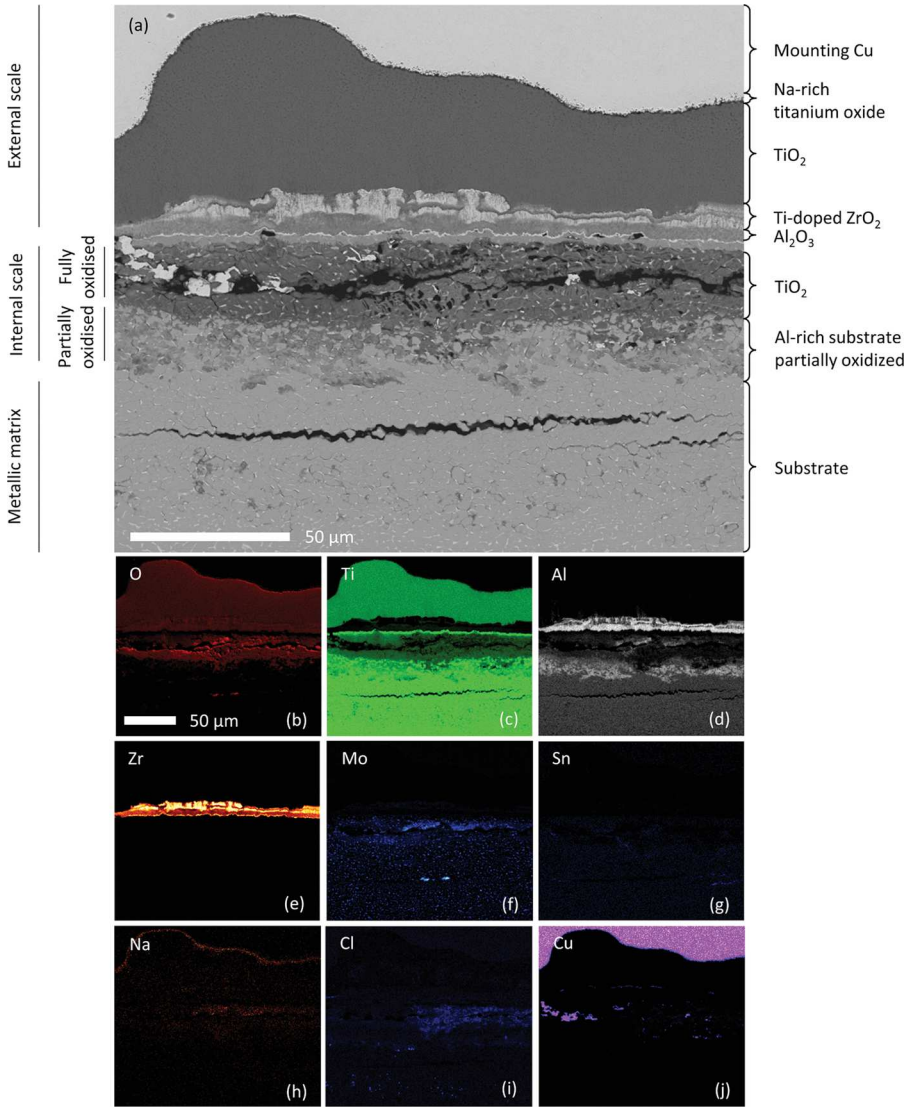

Fig. 6. Cross-section micrograph of sample NA oxidised 600 h at 560 °C in laboratory air with NaCl deposit, (a) in BSE contrast and corresponding X-ray maps of O (b), Ti (c), Al (d), Zr (e), Mo (f), Sn (g), Na (h), Cl (i) and Cu (j) elements.

progress. Only a part of each grain has this lath-like structure, while the rest exhibits the metallic aspect that can be seen in the lower part of Fig. 8a. This microstructure suggests that the grains located in the partially oxidised area are composed of both fully oxidised parts and metallic parts. The relative evolution of the oxygen profile acquired in the partially oxidised area (Fig. 7), can also be discussed. Indeed, since the grains composing it are partially oxidised, the high O contents found – which would normally indicate the presence of an oxygen dissolution area – might also result from an average between the O content of both oxidised and un-oxidised regions. Thus, it is rather difficult to exclude or confirm the presence of oxygen dissolution areas.

3.3.2. *TEM detailed characterisation of the internal oxidation area*

In order to get more information concerning the specific and unusual microstructure of the internal oxidation area, a detailed TEM analysis was performed.

Fig. 9a shows a SEM micrograph in BSE contrast of the internal oxidation area. Two different oxide morphologies can be noticed on this micrograph: intragranular oxides (represented by equiaxed partially oxidised grains) followed by a region of intergranular oxidation (with oxidised grain boundaries). The selected area for FIB TEM lamellae sample preparation is denoted by the light blue rectangle that contains the different regions of interest (ROI). Two ROI were investigated denoted as region 1 and region 2. Fig. 9b presents a low magnification image of the TEM lamellae observed in Scanning TEM (STEM) bright field (BF) mode with the two ROI that were investigated.

3.3.2.1. Region 1: intragranular oxidation area. A high magnification TEM bright field (TEM-BF) image of region 1 is shown in Fig. 10. This region of the sample consists of laths (grey areas) formed in the metal matrix (black areas) with some voids (white areas). Regions where EDS (yellow), EELS (green) and ED (orange) analyses were performed are also reported in Fig. 10.

Fig. 11a was obtained using high-angle annular dark field STEM-HAADF imaging mode. Using this mode, the image contrast depends on the atomic number (Z) where the brighter and darker regions correspond to higher and lower Z, respectively.

Fig. 11b presents the results of EDS analyses. It can be noticed an alternating elemental composition between Ti and O as the analysis passes from the bright to dark regions. The atomic concentration of O and Ti is around 62.2 at. % and 27.5 at. % respectively in the dark regions that would indicate the presence of TiO_2. Thus, bright regions would correspond to the remaining metallic matrix, more or less enriched in O (from 20 to 30 at. %). Al has a mean value concentration of

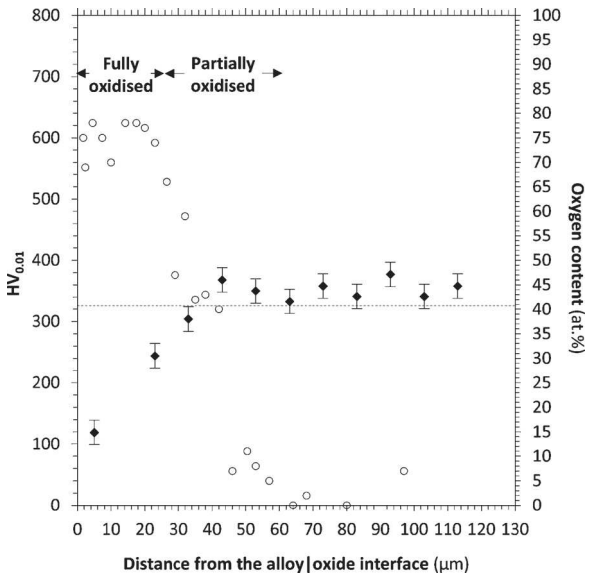

Fig. 7. Micro-hardness (◆) and relative oxygen content (○) (obtained by EDS) profiles versus distance from the alloy|oxide interface of sample NA, oxidised 600 h at 560 °C in laboratory air with NaCl deposit.

13 at. % and 7 at. % along the metallic and oxidised regions, respectively. The other elemental concentrations such as Mo, Sn, Si and Zr are present in very low percentages (below 2.5 at. %). However, neither Na nor Cl were detected by EDS.

These results are confirmed by EELS analyses, whose ELNES spectra are presented in Fig. 11c. In 3d transition metals, such as Ti, ELNES spectra are identified by L_3 and L_2 white lines that represent the spin-orbit splitting of 2p core hole and transition to 3d states (L_3 from $2p_{3/2} \rightarrow 3d$ and L_2 from $2p_{1/2} \rightarrow 3d$) [34,35]. Metallic Ti-L_3 and L_2 white lines are usually detected at 457 and 462.5 eV [36,37]. Ti bonding with O to form oxides, leads to a split in the L_2 and L_3 white lines and four peaks are detected instead of two. This is because of the octahedral coordination of Ti with O, splitting the degenerated unoccupied 3d states to lower t_{2g} and higher e_g bands [38–41]. As the line profile passes from bright to dark regions in Fig. 11a, the intensity and ELNES position of Ti-L_3 and L_2 edges change along with a decrease in intensity and profile change of O-K edge. This change corresponds to an alternation between metallic and oxidised Ti. For example, ELNES spectrum 9 reflects the metallic characteristic of Ti-$L_{2,3}$ white lines with no detection of O-K edge. However, in ELNES spectrum 8, the Ti-$L_{2,3}$ edges is shifted to higher energy loss values where L_2 and L_3 white lines split to lower t_{2g} and higher e_g bands denoted by 'a' and 'b'. This change in ELNES spectrum of Ti is accompanied by an increase in O-K edge intensity. Similarly to EDS results, neither Na nor Cl were detected by EELS.

To get more information on the formation of the oxidised laths, SA EDS analyses have been done at the end tale of one lath denoted by small circles in Fig. 10 and summarized in Table 4. If position 10 EDS spectrum confirms the presence of Ti oxide, spectra acquired along the lath growth direction and on each side of this direction do not put in evidence any noticeable composition difference between both zones.

EELS technique can also give access to the oxidation state of the analysed elements, through the fingerprint approach based on the fine structure. The positions of Ti-$L_{2,3}$ edges were then compared with values obtained in previous studies [40,42,43]. On EELS spectrum 8 (Fig. 11c), Ti-$L_{2,3}$ edges are compared with a previous study on Ti-6Al-2Sn-4Zr-2Mo-Si oxidised in synthetic air, where a rutile TiO_2 scale grew on the alloy and was identified by EELS and SAED techniques [37]. The comparison of Ti-$L_{2,3}$ ELNES fine structure of spectrum 8 with the work of Abdallah et al. [37] revealed that the oxide has an anatase structure due to a difference in shape and to a change in position to slightly lower energy loss value of 'b' peak [40].

Presence of metallic Ti and anatase TiO_2 is confirmed by SAED whose patterns are presented in Fig. 12a and b respectively. ED1 and ED2 patterns were observed using nano-diffraction method. ED1 corresponds to HCP-Ti structure along [$\bar{1}$, 2, $\bar{1}$, 0] zone axis (ZA) with measured interplanar distances. ED2 obtained inside a lath shows a polycrystalline structure of anatase TiO_2 (JCPDS n° 00-021-1272).

The interface between metallic Ti (dark) and a TiO_2 lath (light grey) is presented in a high magnification TEM image (Fig. 13). The α-Ti matrix appears, at this scale of a grain, to be monocrystalline. However, the TiO_2 lath seems to be composed of several small crystallites of 7 nm diameter in average, according to the small coherence domains denoted by the colored circles. Moreover, the TiO_2 lath obviously appears to follow a specific growth direction within the α-Ti matrix, parallel to (001) planes, according to the measured interplanar distance of 4.7 Å. However, any orientation relationship between the α-Ti matrix and the TiO_2 lath crystallites cannot be clearly evidenced.

3.3.2.2. Region 2: intergranular oxidation area. This second region was located deeper in the metallic matrix, just beneath region 1. Fig. 14 presents a low magnification STEM-HAADF image that highlights the regions of ED, EDS and EELS line profile analyses.

A zoom on the EDS region is shown in Fig. 15a, where five areas

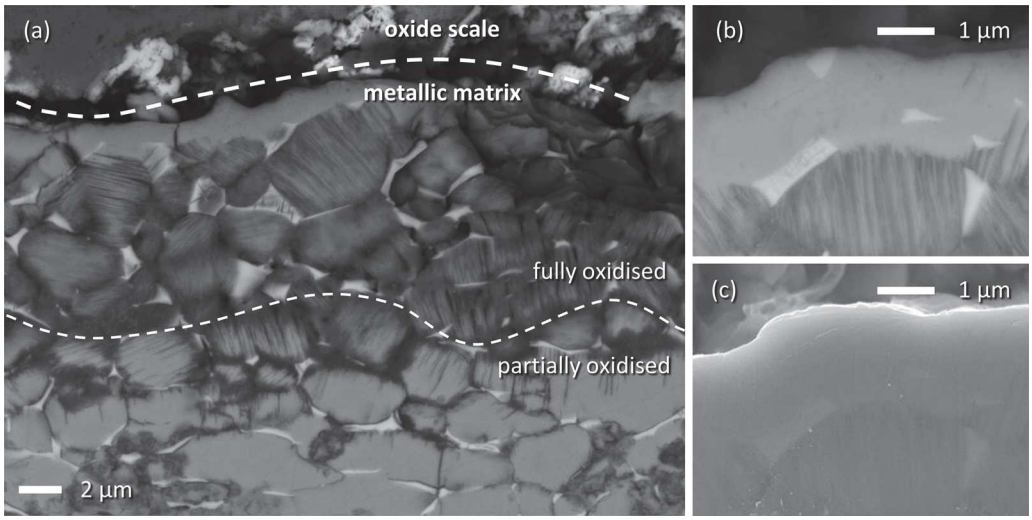

Fig. 8. Global SEM micrograph in BSE contrast of the first stages of internal oxidation in sample NA (a), and zoom on an α-phase grain partially oxidised in BSE (b) and SE (c) contrasts.

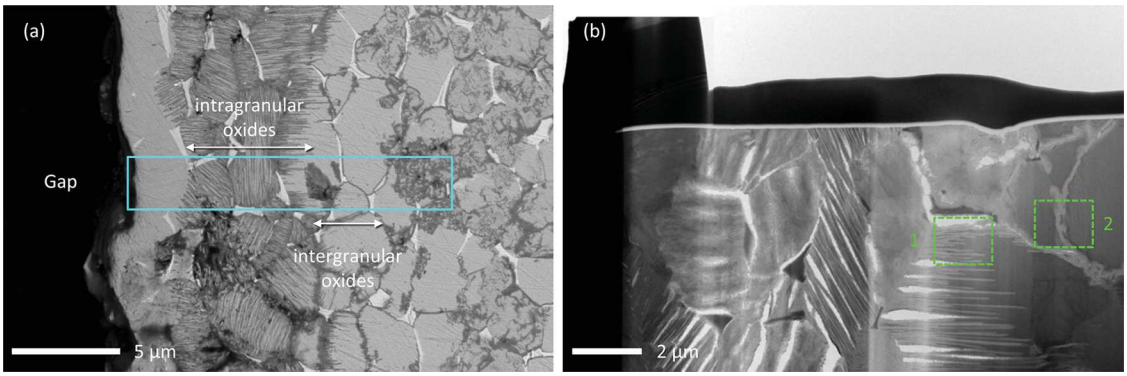

Fig. 9. SEM micrograph of the sample surface showing in light blue the selected area for a cross sectional TEM lift out lamellae prepared by FIB (a), and low magnification STEM-BF micrograph showing the two regions to be analysed (b). (For interpretation of the references to colour in this figure legend, the reader is referred to the web version of this article).

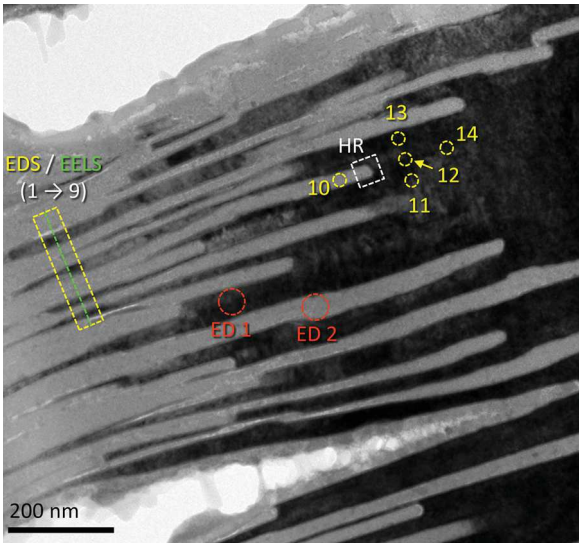

Fig. 10. Low magnification of region 1 where the different zones of EDS (yellow rectangle and circles), EELS (green line), ED (orange circles) and HR (white rectangle) analyses are denoted. (For interpretation of the references to colour in this figure legend, the reader is referred to the web version of this article).

were selected for the analysis. According to EDS results (Fig. 15b), the small precipitate analysed in EDS spectrum 15 reflects a composition close to Ti_3Al, known to be a brittle phase. EDS spectra 16 and 18 give the elementary composition inside the grain boundary, where high concentration of O is detected (around 60 at. %) reflecting TiO_2 composition, whereas EDS spectra 17 and 19 give the elementary compositions of the α-Ti matrix.

Table 4
Atomic composition of the SA EDS points in Fig. 10.

Position	Content (at. %)						
	O	Al	Si	Ti	Zr	Mo	Sn
10	44.4	9.5	0.6	43.7	0.2	1.0	0.6
11	7.0	11.2	0.4	78.5	1.5	0.7	0.8
12	7.5	11.0	0.5	77.9	1.6	0.7	0.8
13	8.2	10.8	0.6	77.7	1.2	0.7	0.8
14	6.4	10.6	0.6	79.0	1.9	0.7	0.7

Fig. 16 presents the ELNES spectra at Ti-$L_{2,3}$ and O-K edges acquired from the alloy towards the grain boundary. In the alloy (ELNES spectra 10 and 17), metallic Ti-$L_{2,3}$ edges are present with no detection of O-K edge. Inside the grain boundary (ELNES spectra 13 and 14), along with an O-K edge, Ti-$L_{2,3}$ white lines split to have in total four peaks, the same signature as TiO_2 presented in region 1. At the interface between the alloy and grain boundary (ELNES spectra 12, 15 and 16), a change in shape and position of Ti-$L_{2,3}$ edges can be also noticed, showing the transition between metallic Ti and TiO_2. ELNES spectrum 11 corresponding to the precipitate that was identified as Ti_3Al has a signature similar to metallic Ti.

Additionally, ED was performed in the alloy (ED3 region in Fig. 14) and the grain boundary (ED4 region in Fig. 14), of which diffraction patterns are shown in Fig. 17. The α-Ti structure is shown in Fig. 17a along [0,1, $\bar{1}$, 2] ZA. Again, polycrystalline structure of anatase TiO_2 is identified in Fig. 17b overlayered with HCP matrix spots.

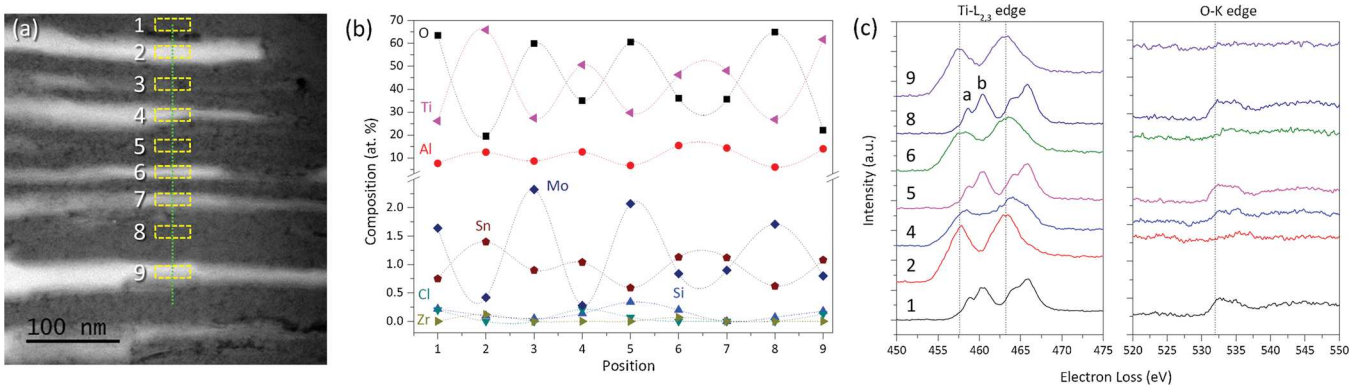

Fig. 11. STEM-HAADF micrograph of the ROI in Fig. 10 with the yellow rectangular boxes indicating the EDS regions and the green dashed line the EELS line profile location. (a) Corresponding elementary EDS compositions and (b) ELNES spectra of Ti-$L_{3,2}$ and O-K edges. (For interpretation of the references to colour in this figure legend, the reader is referred to the web version of this article).

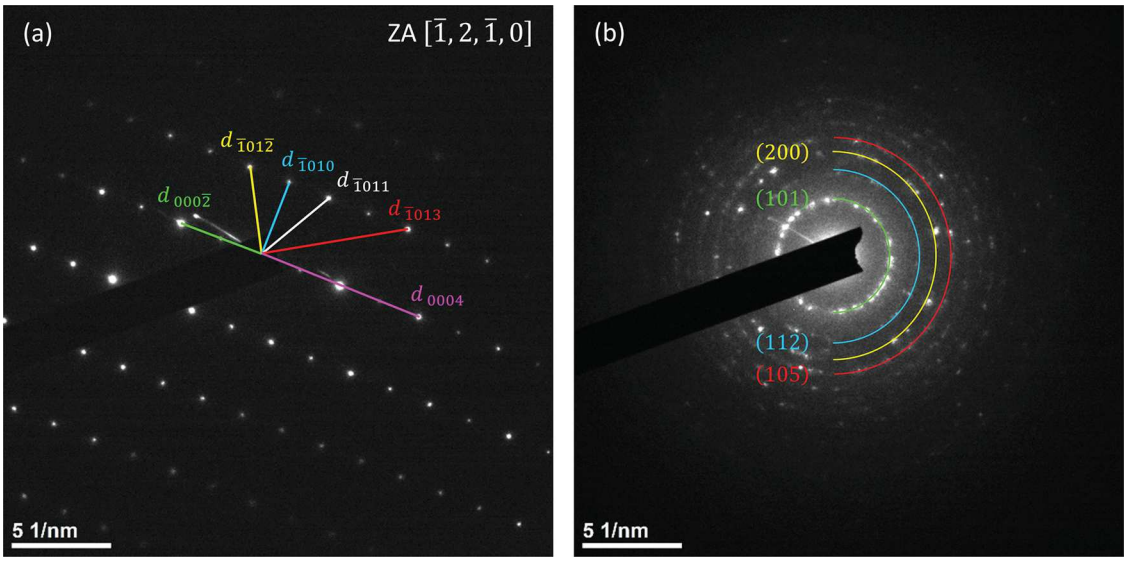

Fig. 12. Electron diffraction (ED1) of α-Ti along [1̄, 2, 1̄, 0] ZA (a) and ED2 of anatase TiO_2.

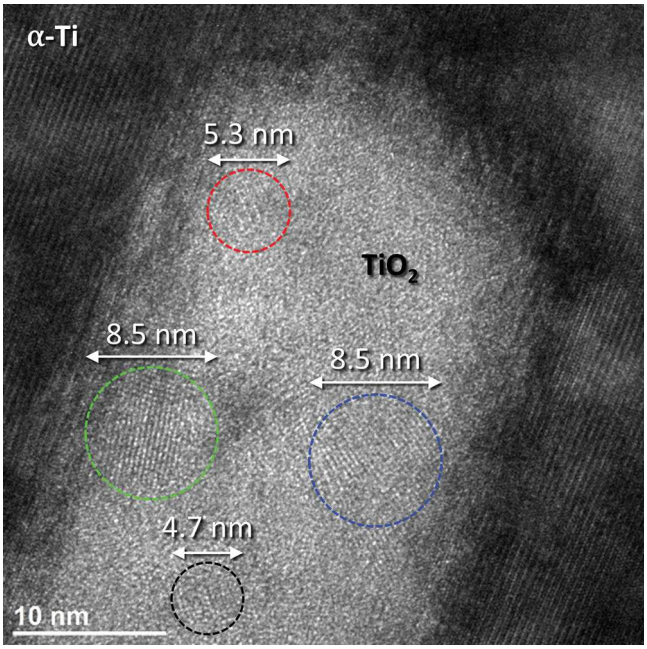

Fig. 13. High magnification TEM image of a TiO_2 lath apex surrounded the α-Ti matrix.

All results obtained on both samples A and NA are summarized in Table. 5.

4. Discussion

4.1. Oxidation in absence of NaCl deposit

In laboratory air (sample A), oxidation of Ti-6Al-2Sn-4Zr-2Mo-Si alloy for 600 h at 560 °C led to a weight gain per unit area of 0.28 ± 0.10 mg.cm^{-2}. This slight mass increase is consistent with the parabolic rate kinetics reported by Dupressoire et al. [11]. Corrosion products were mainly rutile and anatase TiO_2, in agreement with previous observations [11]. However, Dupressoire et al. [11] also reported the presence of Al_2O_3 after 100 h oxidation at 650 °C using fluorescence spectroscopy, although, it was not detectable by XRD, like in the present study. This is certainly due to its relatively low content as compared to that of TiO_2 phase. Similarly, Berthaud et al. [17] also reported by XPS analysis the presence of Al_2O_3 at the top of the oxide scale formed on a sample oxidised 100 h at 560 °C. Finally, our results regarding oxide scale thickness (approximately 0.2 μm) and oxygen dissolution area (OAZ) thickness (approximately 10 μm by EDS and approximately 25 μm by micro-hardness) are consistent with previous results obtained by McReynolds and Tamirisakandala [15]. Their EDS results, obtained on a sample oxidised 500 h at 649 °C, suggest that the oxide scale would be mainly composed of Ti-oxide with small amounts of Al- and Zr-oxides.

4.2. Corrosion in presence of NaCl deposit: formation of an external corrosion scale

The presence of a NaCl deposit was shown to be extremely harmful for the material in laboratory air (NA) at 560 °C; the weight gain per unit area (3.41 ± 0.12 mg.cm^{-2}) being 12 times higher than for NaCl-free sample (A). This detrimental effect of NaCl deposit on the oxidation resistance of pure Ti and Ti-alloys has already been reported in several studies [10,19–21,24,25]. The loss in corrosion resistance in presence of NaCl deposit is thought to be related to an active corrosion mechanism. This mechanism would rely on the initial reaction of native TiO_2 with NaCl to form a mixed sodium-titanium oxide and volatile chlorine, which would then diffuse trough the scale and react with the metallic substrate to form volatile Ti chlorides that will be thereafter oxidised to form Ti oxides [10,20,24,25,30]. The huge depletion of Ti in the internal oxidation area would attest to such an active oxidation process. Thermodynamic calculations performed in a previous study [10] showed that this mechanism can be activated because of the high vapour pressure of the $NaCl_{(g)} \leftrightarrow NaCl_{(s)}$ equilibrium at high temperature, which can reach 3×10^{-7} bar at 560 °C [10,44,45].

The as-described active corrosion mechanism allows explaining the formation of thick TiO_2 layers during high temperature exposure in presence of NaCl. Nevertheless, in the case of Ti-6Al-2Sn4Zr-2Mo-Si alloy, the corrosion scale equally contains Zr and Al-based oxides. It is obvious that the mechanism needs to be adapted in order to take into account Zr and Al contributions. Since Sn, Mo and Si oxides are not present in the external oxide layer (as shown in Fig. 6 for Sn and Mo), the reactions involving Sn, Mo and Si are not taken into account in the mechanism. Thus, based on the present experimental results and on the mechanisms previously proposed for other Ti-based alloys, the corrosion of Ti-6Al-2Sn-4Zr-2Mo-Si alloy in laboratory air with NaCl deposit (NA) would be based on the following series of reactions, supported by

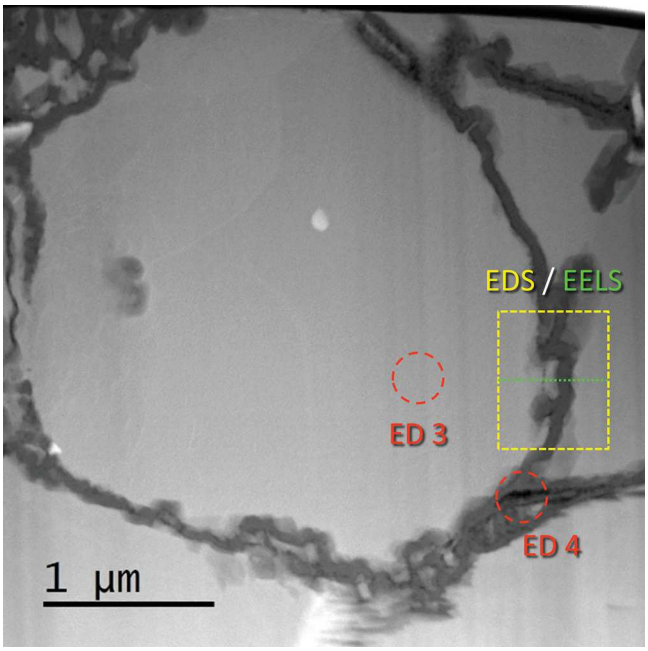

Fig. 14. Low magnification STEM-HAADF micrograph of region 2, where EDS/EELS and ED analyses were performed.

thermodynamics calculations presented in Table 6.

The first step would be initiated by the reaction of the NaCl $_{(g)}$ vapour with the native TiO_2 in presence of $O_{2\,(g)}$ (Eq. (1)).

$$4\,NaCl_{(g)} + O_{2\,(g)} + 5\,TiO_{2\,(s)} \leftrightarrow Na_4Ti_5O_{12\,(s)} + 2\,Cl_{2\,(g)} \quad (1)$$

The $Cl_{2\,(g)}$ formed would then migrate through the damaged oxide scale, down to the alloy|oxide interface, and react with the alloying elements to form the corresponding metal chlorides, as described in Eq. (2), Eq. (3) and Eq. (4) below and in Table 6.

$$\frac{1}{2}\,Ti_{(s)} + Cl_2 \leftrightarrow \frac{1}{2}\,TiCl_{4\,(g)} \quad (2)$$

$$\frac{2}{3}\,Al_{(s)} + Cl_{2\,(g)} \leftrightarrow \frac{2}{3}\,AlCl_{3\,(g)} \quad (3)$$

$$\frac{1}{2}\,Zr_{(s)} + Cl_{2\,(g)} \leftrightarrow \frac{1}{2}\,ZrCl_{4\,(g)} \quad (4)$$

The as formed metal chlorides will then diffuse throughout the oxide scale and will be oxidised in locations where the oxygen partial pressure $P(O_2)$ reaches a critical value inducing chloride oxidation. Chloride oxidation reactions are presented in Eq. (9), Eq. (10) and Eq. (11) below.

$$TiCl_{4\,(g)} + O_{2\,(g)} \leftrightarrow TiO_{2\,(s)} + 2\,Cl_{2\,(g)} \quad (9)$$

$$\frac{4}{3}\,AlCl_{3\,(g)} + O_{2\,(g)} \leftrightarrow \frac{2}{3}\,Al_2O_{3\,(s)} + 2\,Cl_{2\,(g)} \quad (10)$$

$$ZrCl_{4\,(g)} + O_{2\,(g)} \leftrightarrow ZrO_{2\,(s)} + 2\,Cl_{2\,(g)} \quad (11)$$

As all the reactants of Eq. (9), Eq. (10) and Eq. (11) are in gaseous state, it is important to mention that because of the heterogeneous nucleation principle, these reactions of chloride oxidation will preferentially take place on any defect (i.e. material surface, pore surface or crack surface) that would favour them energetically, similarly to what occurs in chemical vapour deposition (CVD) processes. They should therefore lead to the formation of massive products such as oxide layers instead of powders.

Furthermore, depending on local oxygen partial pressure $P(O_2)$ and chlorine partial pressure $P(Cl_2)$, each metal chloride will be oxidised when specific critical values of $P(O_2)$ will be reached. These specific critical values of $P(O_2)$ depend on the equilibrium $P(O_2)$ of each chloride oxidation reaction (for a given $P(Cl_2)$). Thus, respective oxides will form at different locations of the oxide scale, leading to its stratification as a function of respective equilibrium $P(O_2)$ values of each chloride oxidation reaction. Based on this mechanism, the initial layer of $Na_4Ti_5O_{12}$ that composes the surface of the oxide scale would be followed by a TiO_2 scale representing the main part of the oxide scale, then followed by an intermediate layer of ZrO_2 and a final layer of Al_2O_3 in the innermost part of the oxide scale. Fig. 18 presents an overlay of the theoretical predominance diagrams of all the alloying elements (Ti, Al, Sn, Zr, Mo and Si) calculated for pure constituents at 833 K. Knowing that the activity of alloying elements is lower than 1, all horizontal and vertical equilibrium lines of the predominance diagram should be shifted respectively upward and rightward. However, diagonal equilibrium lines should not be significantly shifted as they do not directly depend on the activity of their respective metallic element. The present predominance diagram, especially the sequence of diagonal equilibrium lines, should therefore be suitable for predicting the sequence of oxides precipitation in the present system.

According to Fig. 18, various oxides should have been experimentally observed beneath the first $Na_4Ti_5O_{12}$ scale: namely MoO_3, SnO_2, TiO_2, ZrO_2, SiO_2 and Al_2O_3. In practice, only TiO_2, ZrO_2 and Al_2O_3 were

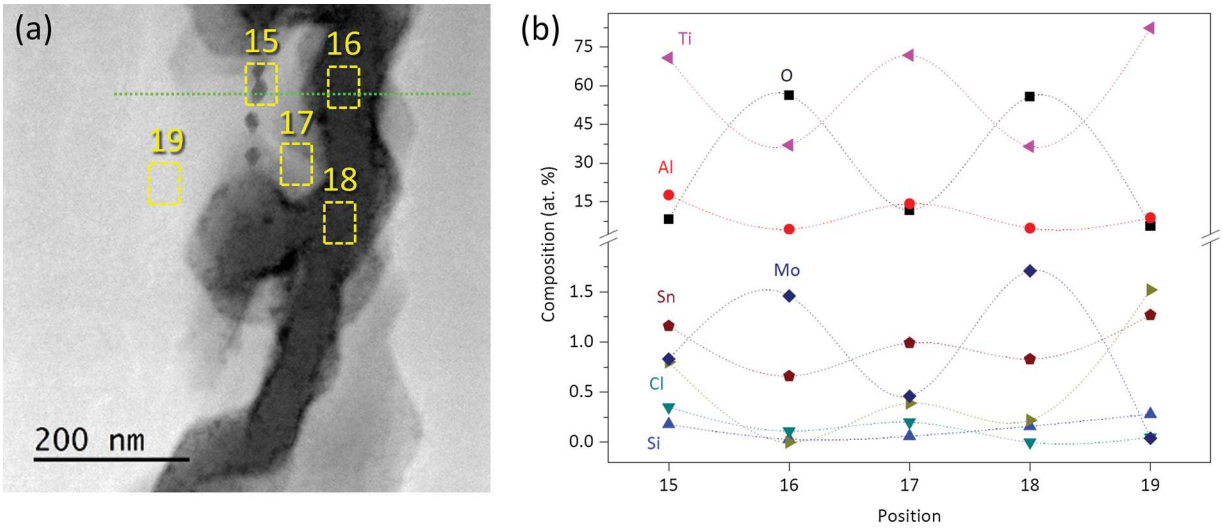

Fig. 15. STEM-HAADF micrograph of the ROI in Fig. 14 with the yellow rectangular boxes indicating the EDS regions in (a) and the elementary compositions in (b). (For interpretation of the references to colour in this figure legend, the reader is referred to the web version of this article).

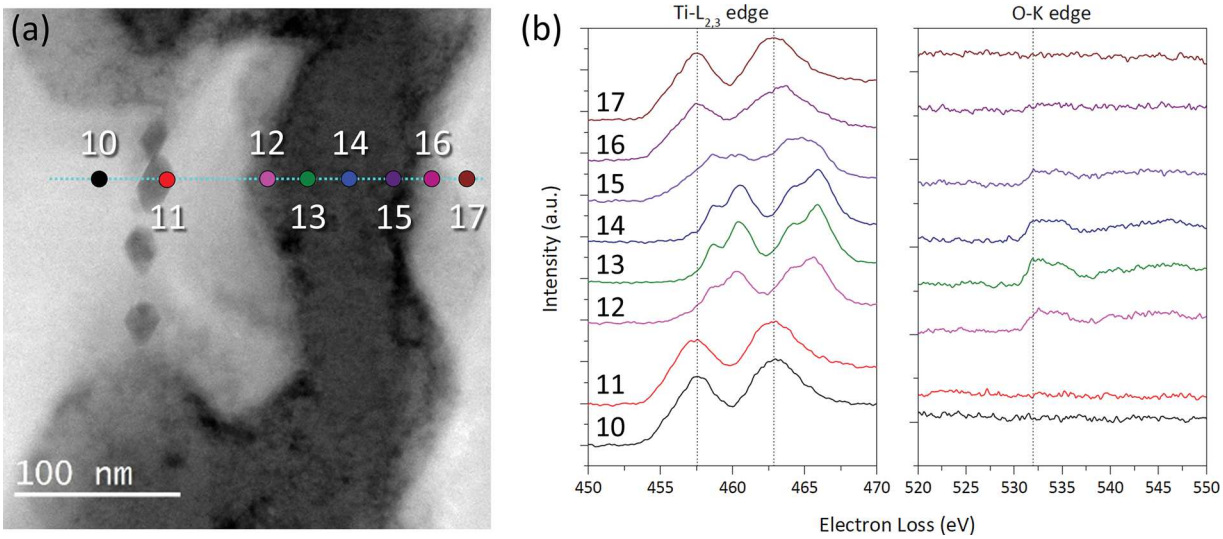

Fig. 16. STEM-HAADF micrograph of the EELS line profile (a) and its corresponding ELNES spectra (b).

observed beneath $Na_4Ti_5O_{12}$ top layer. A diagram of the reaction scheme proposed for the formation of such a stratified oxide scale is presented in Fig. 19. Despite the fact that formation of some Sn, Mo and Si oxides is thermodynamically allowed, the absence of Sn and Mo oxide layers in the external corrosion scale might be explained by the very low stability of their respective chlorides as compared to Ti, Al and Zr chlorides. The high volatility of MoO_3 might also explain its absence at the top of the external oxide layer. The very low content of Si initially present in the Ti-6Al-2Sn-4Zr-2Mo-Si alloy might explain the absence of a continuous Si oxide layer, or the failure to detect it if, nonetheless, it exists.

4.3. Corrosion in presence of NaCl deposit: formation of an internal corrosion area

Despite the fact that internal oxidation of Ti is usually unexpected, the similarity between the microstructure shown in Fig. 10a and the initial metallic matrix suggests that metallic grains are converted into oxide grains through a direct oxidation process and do not result from the oxidation of metal-chlorides, as explained above to occur for the external oxide scale formation. Additionally, it can be supposed that α-grains oxidize preferentially as compared to β-grains, due to the higher solubility of O in the α-phase.

In agreement with Fan et al. [19,22], the internal oxidation area was found to be composed of TiO_2 and α-Ti matrix more or less enriched in O. However, SAED analyses performed in the present work revealed that Ti oxide was actually nanocrystalline anatase TiO_2 rather than rutile TiO_2. As a rutile to anatase transition can occur if the grain size drops down below 17 nm [46], the TiO_2 crystallites size, which was found to be lower than 10 nm, might explain the stability of anatase instead of rutile.

Based on the relative stability of each alloying elements oxide (Fig. 18), the TiO_2 composing the internal oxidation area (that forms beneath ZrO_2 and Al_2O_3 layers of the external oxidation scale) should not be the most stable at this location. The anatase structure of TiO_2 might be an explanation for its unexpected stability at this location.

Furthermore, EDS and EELS analyses revealed that, if O dissolves in the metallic parts remaining between the TiO_2 laths, no sign of O dissolution was found downstream of the laths growing-front. This result would attest on the preponderance of the active oxidation kinetics over that of oxygen dissolution and inward diffusion. However, O content obviously appears to be important enough to allow the oxidation of the

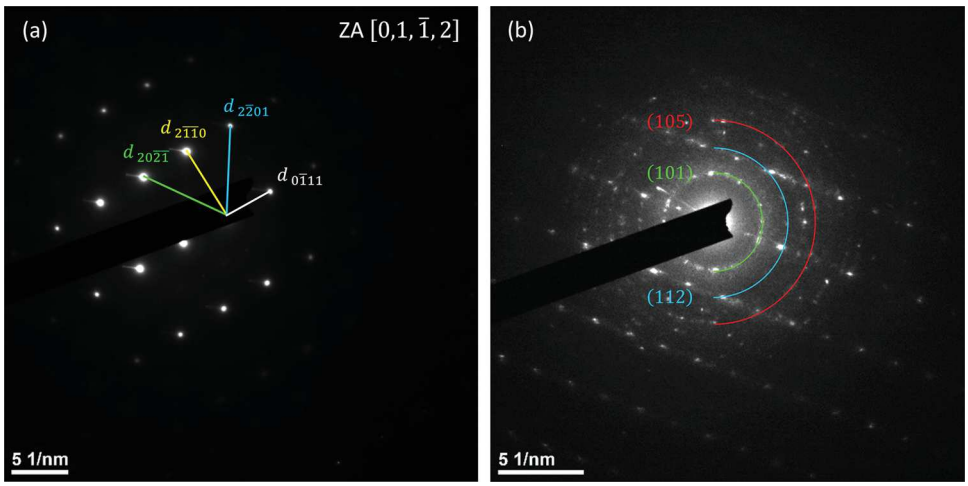

Fig. 17. Electron diffraction in an α-Ti grain (ED3) for HCP Ti along [0,1, $\bar{1}$, 2] ZA (a) and ED4 in the neighboring grain boundary showing anatase TiO_2 polycrystalline structure, overlayered with ED spots of α-Ti matrix.

Table 5
Summary of the results obtained for the different oxidation conditions at 560 °C after 600 h exposures.

			Air (sample A)	Air + NaCl deposit (sample NA)
		Weight gain per unit area ($mg.cm^{-2}$)	0.28 ± 0.10	3.41 ± 0.12
External oxide		Thickness (μm)	0.2	50
		Composition	TiO_2 (rutile + anatase)	$Na_4Ti_5O_{12}$ TiO_2 (rutile) Ti-doped ZrO_2 Al_2O_3
		Morphology	dense	porous blistered cracked
Internal oxide	Fully oxidised area	Thickness (μm)	/	25
		Composition	/	TiO_2 (anatase)
		Morphology	/	cracked with grain ravelling
	Partially oxidised area	Thickness (μm)	/	35
		Composition	/	TiO_2 (anatase)
		Morphology	/	cracked
OAZ		Thickness (μm)	10 (EDS) 25 ($HV_{0.01}$)	/

Table 6
Reactions proposed for the active corrosion mechanisms and their corresponding calculated values of standard free enthalpy (calculated with FactSage 6.4 using reaction module and FactPS / FT Oxid and FTSalt databases).

No.	Equilibrium equation	ΔG^0_{833K} ($kJ.mol^{-1}$)
(1)	$4\,NaCl_{(g)} + O_{2\,(g)} + 5\,TiO_{2\,(s)} \leftrightarrow Na_4Ti_5O_{12\,(s)} + 2\,Cl_{2\,(g)}$	/
(2)	$\frac{1}{2}\,Ti_{(s)} + Cl_{2\,(g)} \leftrightarrow \frac{1}{2}\,TiCl_{4\,(g)}$	−331.26
(3)	$\frac{2}{3}\,Al_{(s)} + Cl_{2\,(g)} \leftrightarrow \frac{2}{3}\,AlCl_{3\,(g)}$	−362.05
(4)	$\frac{1}{2}\,Zr_{(s)} + Cl_{2\,(g)} \leftrightarrow \frac{1}{2}\,ZrCl_{4\,(g)}$	−387.03
(5)	$Sn_{(s)} + Cl_{2\,(g)} \leftrightarrow SnCl_{2\,(g)}$	−219.81
(6)	$\frac{1}{2}\,Sn_{(s)} + Cl_{2\,(g)} \leftrightarrow \frac{1}{2}\,SnCl_{4\,(g)}$	−190.68
(7)	$\frac{1}{2}\,Mo_{(s)} + Cl_{2\,(g)} \leftrightarrow \frac{1}{2}\,MoCl_{4\,(g)}$	−150.68
(8)	$\frac{1}{2}\,Si_{(s)} + Cl_{2\,(g)} \leftrightarrow \frac{1}{2}\,SiCl_{4\,(g)}$	−276.25
(9)	$TiCl_{4\,(g)} + O_{2\,(g)} \leftrightarrow TiO_{2\,(s)} + 2\,Cl_{2\,(g)}$	−129.86
(10)	$\frac{4}{3}\,AlCl_{3\,(g)} + O_{2\,(g)} \leftrightarrow \frac{2}{3}\,Al_2O_{3\,(s)} + 2\,Cl_{2\,(g)}$	−219.01
(11)	$ZrCl_{4\,(g)} + O_{2\,(g)} \leftrightarrow ZrO_{2\,(s)} + 2\,Cl_{2\,(g)}$	−164.59
(12)	$SnCl_{2\,(g)} + O_{2\,(g)} \leftrightarrow SnO_{2\,(s)} + Cl_{2\,(g)}$	−187.19
(13)	$SnCl_{4\,(g)} + O_{2\,(g)} \leftrightarrow SnO_{2\,(s)} + 2\,Cl_{2\,(g)}$	−25.63
(14)	$\frac{2}{3}\,MoCl_{4\,(g)} + O_{2\,(g)} \leftrightarrow \frac{2}{3}\,MoO_{3\,(s)} + \frac{4}{3}\,Cl_{2\,(g)}$	−155.21
(15)	$SiCl_{4\,(g)} + O_{2\,(g)} \leftrightarrow SiO_{2\,(s)} + 2\,Cl_{2\,(g)}$	−201.30

grain boundaries and of the matrix depleted in metallic elements. Indeed, because of the active oxidation loop, Ti, Al and Zr would be consumed in the grain boundaries first, followed by the α-grains, leading to a significant decrease in their activity inside the depleted regions. However, if these alloying elements are assumed to be transported outward under a gaseous form (metal chloride), the present EDS and EELS results do not allow to identify whether Cl is carried inward through gaseous diffusion ($Cl_{2\,(g)}$) or solid-state diffusion (Cl^-). Due to the inward O flow (arriving through the numerous cracks and short circuit diffusion paths present in both external and internal oxide areas), the local O activity appears to become sufficient to induce the oxidation of the remaining metallic elements. The formation of nanocrystalline anatase TiO_2 might be due to a fast oxidation process, promoted by the fast consumption of metallic elements by the active oxidation process at the upper part of the alloy, in relation to their very important depletion at this location. Fig. 20 presents a schematic representation of formation of the internal oxidation area.

If the preferential oxidation of grain boundaries seems rather obvious, the explanation for the unusual directional growth of TiO_2 laths within the α-grains appears unclear. The high magnification TEM image of the TiO_2 lath apex (Fig. 13) revealed that the growth direction of these laths is parallel to the basal planes of α-Ti. However, EDS analyses downstream and on each side of a TiO_2 lath apex did not allow to evidence any chemical heterogeneity within a same α-grain that might explain such a reactivity difference between the oxidised and unoxidised regions. Moreover, this inhomogeneous and directional internal oxidation appears to be not systematic. Indeed, it did not seem to be observed on pure Ti [24], or some other Ti alloys [10,25]. However, it is surprisingly similar to formation and growth of α-phase grain boundaries and Widmanstätten laths encountered in a β-Ti matrix [47]. The present inhomogeneous internal oxidation phenomenon might therefore be due to some structural heterogeneities, inherited from the thermo-mechanical history of the sample, and fortuitously revealed by the active oxidation process.

5. Conclusion

A large increase in high-temperature corrosion rate was observed for Ti-6Al-2Sn-4Zr-2Mo-Si alloy in presence of solid NaCl deposit. This enhancement is attributed to the presence of $Cl_{2\,(g)}$ coming from NaCl decomposition, which creates an active oxidation loop. In these conditions, corrosion of the material leads to the formation of both external and internal oxidation areas, which is unusual for Ti and Ti alloys.

In the case of Ti-6Al-2Sn-4Zr-2Mo-Si alloy, containing several alloying elements, the active oxidation loop leads to a stratification of the oxide scale. Overlaying the predominance diagrams of each pure alloying element allows, in a first approximation, to predict the stratification of the oxide scale. However, the highly restrained evaluation of the partial pressure of each gaseous species, due to oxide scale cracking, may strongly limit the accuracy of these predictions. Such predictions might be improved by correcting each predominance diagram with the actual activity of each alloying element. Despite the simple and rough nature of the present thermodynamic approximations, quite an accurate prediction was obtained regarding the stratification of the external oxide scale.

Detailed SEM and TEM analyses reveal a two steps formation process for the internal oxidation area. Firstly, grain boundaries of the metallic matrix would be attacked by $Cl_{2\,(g)}$ involved in the active oxidation loop, leading to the oxidation of these grain boundaries. Secondly, $Cl_{2\,(g)}$ attack would extend to α-grains, leading to the formation of Widmanstätten-like TiO_2 laths within the α-grains. EELS and SAED reveal that these Widmanstätten-like TiO_2 laths are composed of nanocrystalline anatase TiO_2 surrounded by O-enriched α-Ti matrix. However, the present results do not allow to identify if the origins of such a heterogeneous internal oxidation phenomenon is of chemical and/or structural nature.

6. Data availability

The raw data required to reproduce these findings cannot be shared at this time as the data also forms part of an ongoing study. The processed data required to reproduce these findings cannot be shared at this time as the data also forms part of an ongoing study.

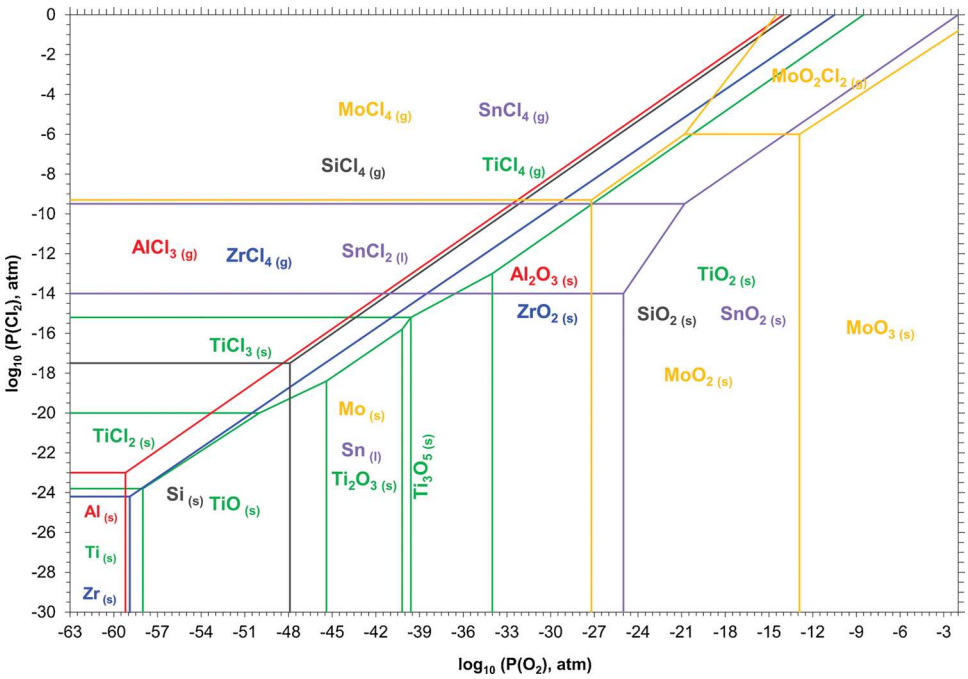

Fig. 18. Overlay of the theoretical predominance diagrams of the Ti, Al, Sn, Zr, Mo and Si elements established for pure constituents at 833 K for 1 atm pressure using FactSage 6.4 from thermodynamic database FactPS / Elem / FT Oxid. Intermediate titanium oxides between Ti_3O_5 and TiO_2 are deliberately not shown for clarity purposes.

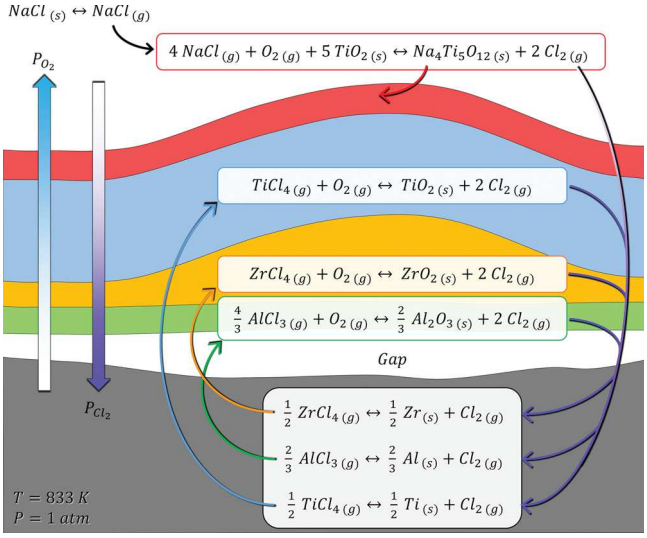

Fig. 19. Diagram of the reaction scheme proposed for the stratification of the external oxide scale formed on sample NA.

Author statement

Clément Ciszak: Conceptualization, Methodology, Validation, Investigation, Data Curation, Writing – Original Draft, Writing – Review and Editing, Visualization **Iman Abdallah:** Validation, Investigation, Data Curation, Writing – Original Draft, Visualization **Ioana Popa:** Conceptualization, Methodology, Validation, Resources, Writing – Review and Editing, Supervision, Project administration, Funding acquisition **Jean-Michel Brossard:** Conceptualization, Methodology, Validation, Formal analysis, Writing – Review and Editing **Aurélie Vande Put:** Resources, Writing – Review and Editing, Supervision, Funding acquisition **Daniel Monceau:** Resources, Writing – Review and Editing, Supervision, Project administration **Sébastien Chevalier:** Resources, Writing – Review and Editing, Supervision, Project administration, Funding acquisition

Declaration of Competing Interest

The authors declare that they have no known competing financial interests or personal relationships that could have appeared to influence the work reported in this paper.

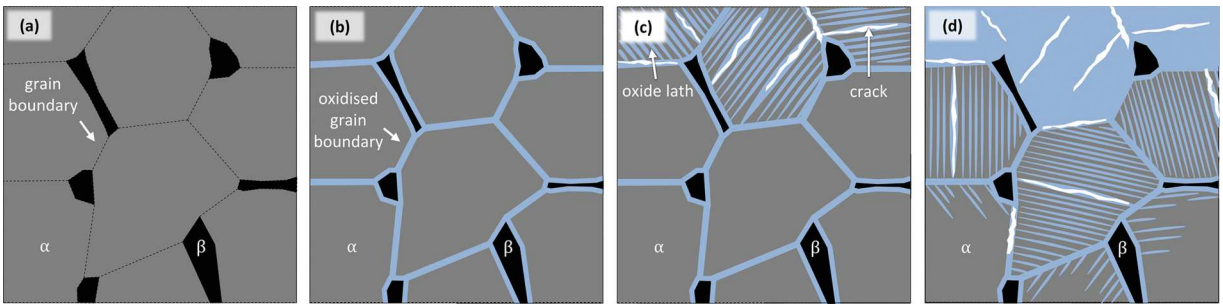

Fig. 20. Schematic representation of formation of the internal oxidation area. (a) Initial state of the metallic matrix. (b) Preferential oxidation of grain boundaries. (c) Growth of oxide laths in the α-grains and formation of crack leading to partially oxidised grains. (d) Growth of the oxide laths leading to the conversion of partially oxidised α-grains into fully oxidised ones and extension to un-oxidised α-grains.

Acknowledgements

This work was financially supported by ICB and CIRIMAT laboratories. Authors thank the 'Fondation de la Maison de la Chimie' for the post-doctorate grant of Iman Abdallah. The authors would also like to thank Frédéric HERBST (SEM/EDS analyses), Nicolas GEOFFROY (XRD analyses) and Nathalie ROUDERGUES (technical support) from the ICB laboratory and Alessandro PUGLIARA (TEM/EDS analyses), Claudie JOSSE (FIB TEM lamellae sample preparation) and Teresa HUNGRIA (TEM/EELS analyses) from the Raimond CASTAING micro-characterisation centre.

Appendix A. Supplementary data

Supplementary material related to this article can be found, in the online version, at doi:https://doi.org/10.1016/j.corsci.2020.108611.

References

[1] H.J. Grabke, E. Reese, M. Spiegel, The effects of chlorides, hydrogen chloride, and sulfur dioxide in the oxidation of steels below deposits, Corros. Sci. 37 (1995) 1023–1043, https://doi.org/10.1016/0010-938X(95)00011-8.
[2] Y. Kawahara, High temperature corrosion mechanisms and effect of alloying elements for materials used in waste incineration environment, Corros. Sci. 44 (2002) 223–245, https://doi.org/10.1016/S0010-938X(01)00058-0.
[3] Titanium | Gerd Lütjering | Springer, n.d. //www.springer.com/la/book/9783540713982 (accessed January 24, 2018).
[4] B. Champin, L. Graff, M. Armand, G. Béranger, C. Coddet, Oxydation des alliages de titane au voisinage des températures d'utilisation dans les turbomoteurs, J. Common Met. 69 (1980) 163–183, https://doi.org/10.1016/0022-5088(80)90052-1.
[5] I. Gurrappa, Mechanism of degradation of titanium alloy IMI 834 and its protection under hot corrosion conditions, Oxid. Met. 59 (2003) 321–322, https://doi.org/10.1023/A:1023044111767.
[6] R. Siab, G. Bonnet, J.M. Brossard, J. Balmain, J.-F. Dinhut, Effect of an electro-deposited yttrium containing thin film on the high-temperature oxidation behaviour of TA6V alloy, Appl. Surf. Sci. 253 (2007) 3425–3431, https://doi.org/10.1016/j.apsusc.2006.07.057.
[7] H.L. Du, P.K. Datta, D.B. Lewis, J.S. Burnell-Gray, High-temperature corrosion of Ti and Ti-6Al-4V alloy, Oxid. Met. 45 (1996) 507–527, https://doi.org/10.1007/BF01046849.
[8] H. Guleryuz, H. Cimenoglu, Oxidation of Ti–6Al–4V alloy, J. Alloys. Compd. 472 (2009) 241–246, https://doi.org/10.1016/j.jallcom.2008.04.024.
[9] H.L. Du, P.K. Datta, D.B. Lewis, J.S. Burnell-Gray, Air oxidation behaviour of Ti-6Al-4V alloy between 650 and 850 °C, Corros. Sci. 36 (1994) 631–642, https://doi.org/10.1016/0010-938X(94)90069-8.
[10] C. Ciszak, I. Popa, J.-M. Brossard, D. Monceau, S. Chevalier, NaCl induced corrosion of Ti-6Al-4V alloy at high temperature, Corros. Sci. 110 (2016) 91–104, https://doi.org/10.1016/j.corsci.2016.04.016.
[11] C. Dupressoire, A. Rouaix- Vande Put, P. Emile, C. Archambeau-Mirguet, R. Peraldi, D. Monceau, Effect of nitrogen on the kinetics of oxide scale growth and of oxygen dissolution in the Ti6242S titanium-based alloy, Oxid. Met. 87 (2017) 343–353, https://doi.org/10.1007/s11085-017-9729-1.
[12] A. Casadebaigt, J. Hugues, D. Monceau, Influence of microstructure and surface roughness on oxidation kinetics at 500–600 °C of Ti–6Al–4V alloy fabricated by additive manufacturing, Oxid. Met. 90 (2018) 633–648, https://doi.org/10.1007/s11085-018-9859-0.
[13] H. Guleryuz, H. Cimenoglu, Surface modification of a Ti–6Al–4V alloy by thermal oxidation, Surf. Coat. Technol. 192 (2005) 164–170, https://doi.org/10.1016/j.surfcoat.2004.05.018.
[14] D. Poquillon, C. Armand, J. Huez, Oxidation and Oxygen Diffusion in Ti–6al–4V Alloy: Improving Measurements During Sims Analysis by Rotating the Sample, Oxid. Met. 79 (2013) 249–259, https://doi.org/10.1007/s11085-013-9360-8.
[15] K.S. McReynolds, S. Tamirisakandala, A study on alpha-case depth in Ti-6Al-2Sn-4Zr-2Mo, Metall. Mater. Trans. A. 42 (2011) 1732–1736, https://doi.org/10.1007/s11661-011-0710-3.
[16] R. Gaddam, B. Sefer, R. Pederson, M.-L. Antti, Oxidation and alpha-case formation in Ti–6Al–2Sn–4Zr–2Mo alloy, Mater. Charact. 99 (2015) 166–174, https://doi.org/10.1016/j.matchar.2014.11.023.
[17] M. Berthaud, I. Popa, R. Chassagnon, O. Heintz, J. Lavková, S. Chevalier, Study of titanium alloy Ti6242S oxidation behaviour in air at 560 °C: effect of oxygen dissolution on lattice parameters, Corros. Sci. (2019), https://doi.org/10.1016/j.corsci.2019.06.004 108049.
[18] N. Vaché, D. Monceau, Oxygen diffusion modeling in titanium alloys: new elements on the analysis of microhardness profiles, Oxid. Met. (2020), https://doi.org/10.1007/s11085-020-09956-9.
[19] L. Fan, L. Liu, Z. Yu, M. Cao, Y. Li, F. Wang, Corrosion behavior of Ti60 alloy under a solid NaCl deposit in wet oxygen flow at 600 °C, Sci. Rep. 6 (2016), https://doi.org/10.1038/srep29019.
[20] Y. Shu, F. Wang, W. Wu, Corrosion behavior of Ti60 alloy coated with a solid NaCl deposit in O_2 plus water vapor at 500-700 °C, Oxid. Met. 52 (1999) 463–473, https://doi.org/10.1023/A:1018864216554.
[21] P. Dumas, C.S. John, NaCl-induced accelerated oxidation of a titanium alloy, Oxid. Met. 10 (1976) 127–134, https://doi.org/10.1007/BF00614242.
[22] L. Fan, L. Liu, Y. Cui, M. Cao, Z. Yu, E.E. Oguzie, Y. Li, F. Wang, Effect of streaming water vapor on the corrosion behavior of Ti60 alloy under a solid NaCl deposit in water vapor at 600 °C, Corros. Sci. 160 (2019) 108177, , https://doi.org/10.1016/j.corsci.2019.108177.
[23] M. Berthaud, Étude Du Comportement De l'alliage De Titane Ti6242S à Haute Température Sous Atmosphères Complexes : Applications Aéronautiques, Thesis, Bourgogne Franche-comté, (2018) (accessed November 29, 2019), http://www.theses.fr/2018UBFCK035.
[24] L. Fan, L. Liu, M. Cao, Z. Yu, Y. Li, M. Chen, F. Wang, Corrosion behavior of pure Ti under a solid NaCl deposit in a wet oxygen flow at 600 °C, Metals. 6 (2016) 72, https://doi.org/10.3390/met6040072.
[25] C. Ciszak, I. Popa, J.-M. Brossard, D. Monceau, S. Chevalier, NaCl-induced high-temperature corrosion of β21S Ti alloy, Oxid. Met. 87 (2017) 729–740, https://doi.org/10.1007/s11085-017-9775-8.
[26] M. Zhang, L. Xin, X. Ding, S. Zhu, F. Wang, Effects Ti/TiAlN composite multilayer coatings on corrosion resistance of titanium alloy in solid NaCl-H_2O-O_2 at 600 °C, J. Alloys. Compd. 734 (2018) 307–317, https://doi.org/10.1016/j.jallcom.2017.11.035.
[27] Z. Yao, M. Marek, NaCl-induced hot corrosion of a titanium aluminide alloy, Mater. Sci. Eng. A. 192–193 (1995) 994–1000, https://doi.org/10.1016/0921-5093(95)03345-9.
[28] S. Joseph, T.C. Lindley, D. Dye, E.A. Saunders, The mechanisms of hot salt stress corrosion cracking in titanium alloy Ti-6Al-2Sn-4Zr-6Mo, Corros. Sci. 134 (2018) 169–178, https://doi.org/10.1016/j.corsci.2018.02.025.
[29] D. Zheng, S. Zhu, F. Wang, The influence of TiAlN and enamel coatings on the corrosion behavior of Ti6Al4V alloy in the presence of solid NaCl deposit and water vapor at 450 °C, Surf. Coat. Technol. 201 (2007) 5859–5864, https://doi.org/10.1016/j.surfcoat.2006.10.038.
[30] Y. Xiong, S. Zhu, F. Wang, Synergistic corrosion behavior of coated Ti60 alloys with NaCl deposit in moist air at elevated temperature, Corros. Sci. 50 (2008) 15–22, https://doi.org/10.1016/j.corsci.2007.06.007.
[31] M. Anuwar, R. Jayaganthan, V.K. Tewari, N. Arivazhagan, A study on the hot corrosion behavior of Ti–6Al–4V alloy, Mater. Lett. 61 (2007) 1483–1488, https://doi.org/10.1016/j.matlet.2006.07.058.
[32] J.-D. Béguin, D. Adrian, J.-A. Petit, J.-P. Rivière, C. Vahlas, S. Vaillant, Improvement of Salt Corrosion Resistance of Titanium Alloys by PVD and CVD Coatings, in: Vienna, Austria, (2007), pp. 59–63 (accessed March 3, 2015), http://www.asminternational.org/content/ASM/StoreFiles/05216G_frontmatter.pdf.
[33] J. Baillieux, D. Poquillon, B. Malard, Relationship between the volume of the unit cell of hexagonal-close-packed Ti, hardness and oxygen content after α-case formation in Ti–6Al–2Sn–4Zr–2Mo–0.1Si alloy, J. Appl. Crystallogr. 49 (2016) 175–181, https://doi.org/10.1107/S1600576715022906.
[34] R.F. Egerton, Electron Energy-Loss Spectroscopy in the Electron Microscope, Springer US, Boston, MA, 2011, https://doi.org/10.1007/978-1-4419-9583-4.
[35] R.D. Leapman, L.A. Grunes, P.L. Fejes, Study of the $L_{2,3}$ edges in the 3d transition metals and their oxides by electron-energy-loss spectroscopy with comparisons to theory, Phys. Rev. B 26 (1982) 614–635, https://doi.org/10.1103/PhysRevB.26.614.
[36] S. Terada, K. Asayama, M. Tsujimoto, H. Kurata, S. Isoda, Chemical shift of Electron energy-Loss near-edge structure on the nitrogen K-Edge and titanium L_3-Edge at TiN/Ti interface, Microsc. Microanal. 15 (2009) 106–113, https://doi.org/10.1017/S1431927609090175.
[37] I. Abdallah, C. Dupressoire, L. Laffont, D. Monceau, A. Vande Put, STEM-EELS identification of TiO_XN_Y, TiN, Ti_2N and O, N dissolution in the Ti2642S alloy oxidized in synthetic air at 650 °C, Corros. Sci. 153 (2019) 191–199, https://doi.org/10.1016/j.corsci.2019.03.037.
[38] R. Brydson, B.G. Williams, W. Engel, H. Sauer, E. Zeitler, J.M. Thomas, Electron energy-loss spectroscopy (EELS) and the electronic structure of titanium dioxide, Solid State Commun. 64 (1987) 609–612, https://doi.org/10.1016/0038-1098(87)90792-7.
[39] F. Hofer, P. Warbichler, A. Scott, R. Brydson, I. Galesic, B. Kolbesen, Electron energy loss near edge structure on the nitrogen K-edge in vanadium nitrides, J. Microsc. 204 (2002) 166–171, https://doi.org/10.1046/j.1365-2818.2001.00946.x.
[40] P.L. Potapov, D. Schryvers, Measuring the absolute position of EELS ionisation edges in a TEM, Ultramicroscopy. 99 (2004) 73–85, https://doi.org/10.1016/S0304-3991(03)00185-2.
[41] A. Gloter, C. Ewels, P. Umek, D. Arcon, C. Colliex, Electronic structure of titania-based nanotubes investigated by EELS spectroscopy, Phys. Rev. B 80 (2009) 035413, , https://doi.org/10.1103/PhysRevB.80.035413.
[42] E. Stoyanov, F. Langenhorst, G. Steinle-Neumann, The effect of valence state and site geometry on Ti $L_{3,2}$ and O-K electron energy-loss spectra of Ti_xO_y phases, Am. Mineral. 92 (2007) 577–586, https://doi.org/10.2138/am.2007.2344.
[43] P.E.T. Ngnekou, M.-C. Lafont, F. Senocq, L. Laffont, B. Viguier, J. Lacaze, Structural characterization of the scale formed on a Ti–46Al–8Nb alloy oxidised in air at 700 °C, Intermetallics. 18 (2010) 226–232, https://doi.org/10.1016/j.intermet.2009.

07.013.
[44] B.H. Zimm, J.E. Mayer, Vapor Pressures, Heats of Vaporization, and Entropies of Some Alkali Halides, J. Chem. Phys. 12 (1944) 362–369, https://doi.org/10.1063/1.1723958.
[45] C.T. Ewing, K.H. Stern, Equilibrium vaporization rates and vapor pressures of solid and liquid sodium chloride, potassium chloride, potassium bromide, cesium iodide, and lithium fluoride, J. Phys. Chem. 78 (1974) 1998–2005, https://doi.org/10.1021/j100613a005.
[46] A.L. da Silva, D. Hotza, R.H.R. Castro, Surface energy effects on the stability of anatase and rutile nanocrystals: a predictive diagram for Nb_2O_5-doped-TiO_2, Appl. Surf. Sci. 393 (2017) 103–109, https://doi.org/10.1016/j.apsusc.2016.09.126.
[47] T. Furuhara, S. Takagi, H. Watanabe, T. Maki, Crystallography of grain boundary α precipitates in a β titanium alloy, Metall. Mater. Trans. A. 27 (1996) 1635–1646, https://doi.org/10.1007/BF02649821.